Deformable Respiratory Motion Correction for Hepatic Rotational Angiography

Alexandra Klugmann[a], Bastian Bier[a], Kerstin Müller[b], Andreas Maier[a], Mathias Unberath[a,c]

[a] *Pattern Recognition Lab, Friedrich-Alexander-Universität Erlangen-Nürnberg*
[b] *Radiological Sciences Lab, Stanford University*
[c] *Computer Aided Medical Procedures, Johns Hopkins University*

Abstract

Cone-beam rotational angiography enables 3D imaging of the hepatic vasculature and is considered beneficial for guidance of transcatheter arterial chemoembolization procedures. Respiratory motion during the rotational acquisition challenges state-of-the-art reconstruction algorithms as intra-scan motion leads to inconsistencies causing substantial blurring and streaking artifacts in uncompensated reconstructions, suggesting the need for motion correction.

We propose an automated method for respiratory motion estimation and compensation based on registration of an initial 3D arterial model to vesselness enhanced 2D projection images. Centerline points of the arterial tree are modeled as B-splines over time, the control point positions of which are optimized using -expansion moves on graph cuts. This approach naturally allows for the estimation of 3D rigid translations as well as non-rigid deformations.

Applied to a pre-clinical and a clinical acquisition, the proposed methods resulted in notable reductions in reprojection error and increased vessel sharpness that are reflected in less streaking and blurring artifact compared to the uncompensated case, implying superior vessel contrast. As the proposed methods are generic, future work will investigate their applicability to related rotational angiography imaging protocols, such as coronary angiography.

Keywords: Discrete optimization, Image Reconstruction, Motion Modeling, Interventional Imaging

1. Introduction

Transcatheter arterial chemoembolization (TACE) is a minimally invasive, catheter-based bridge therapy for hepatocellular carcinoma [1] and metastatic liver tumors [2, 3]. TACE relies on intra-arterial injection of small particles, such as ethiodized oil, cancer medication or gold particles, to artificially occlude vessels that feed the tumor with oxygenated blood [4]. Consequently, accurate knowledge of feeding vessels is key for successful treatment [3, 5]. These vessels are traditionally identified based on 2D fluoroscopy images, i. e., digital subtraction angiography (DSA) [3], that are acquired with interventional C-arm angiography systems. Unfortunately, 2D images su er from the e ects of projective simplification, such as foreshortening and overlapping, that complicate diagnostic assessment.

Modern C-arm scanners, however, are motorized and allow for the acquisition of multiple fluoroscopy images while the X-ray source and detector rotate on a circular orbit around the patient [6]. During X-ray acquisition, the vasculature is selectively contrasted by intra-luminal injection of a contrast agent. This imaging protocol is commonly referred to as cone-beam CT (CBCT) or rotational angiography and allows for 3D reconstruction of the vascular anatomy. Clinical studies comparing CBCT to DSA for identifying feeding vessels suggest that providing physicians with the accurate 3D vascular anatomy is potentially beneficial [5, 7, 8].

However, obtaining high quality reconstructions of the hepatic vasculature from rotational angiography is still challenging due to intra-scan motion that leads to image artifacts in the reconstructed 3D image volumes. The liver is strongly a ected by respiratory motion due to its anatomical proximity to the diaphragm that drives diaphragmatic breathing. Hepatic motion due to respiration is largest along the cranial-caudal patient axis (5 – 25 mm) but has components in anterior-posterior (1 – 12 mm) and in left-right (1 – 3 mm) direction [9].

A common way to circumvent intra-scan respiratory motion is requiring patients to hold their breath [10, 11, 12]. Due to the relatively long acquisition time of about 6 s for a single CBCT scan, residual respiratory motion from imperfect breath-hold is a common corruption mechanism that leads to double edges, streaking, and blurring in uncompensated 3D reconstructions. Consequently, motion correction strategies have to be devised to achieve acceptable image quality.

In literature, many approaches are known that seek to assign motion phases to the acquired images. Assuming that multiple respiration cycles are observed, the phase information can be used to extract consistent images, so-called *bins* or *gates*, that are input to 3D reconstruction algorithms. The phase assignment can be performed using external devices [13], such as respiration belts [14]. However, this requires the use of additional equipment that has to be synchronized to the acquired data. To overcome this limitation, other approaches extract surrogate signals from the acquired projection images directly. These ap-

These authors have contributed equally.
Corresponding author:
Email address: unberath@jhu.edu (Mathias Unberath)

proaches usually exploit that diaphragm motion is highly correlated with respiratory motion [9, 15]. Sonke et al. [16] use the Amsterdam shroud to derive a surrogate signal by horizontally aligning the diaphragm position in all images. These approaches are elegant, as they avoid explicit motion compensation.

Unfortunately, they are not applicable in CBCT angiography since the observed motion patterns are not periodic. When motion compensation is applied, the diaphragm position can be used to directly estimate respiratory motion of the liver. This course of action is particularly well suited for the upper parts of the liver and motion estimation along the cranial-caudal direction [15]. In an animal model, Schäfer et al. show that compensation using the projection domain diaphragm displacement is possible. The method handles large displacements but requires sophisticated segmentation of the 3D anatomy, i. e. the ribcage and the diaphragm, in an uncompensated reconstruction [17]. Bögel et al. [18] automatically track the diaphragm contour in the projection image sequence and use a motion-corrected triangulation approach on the diaphragm vertex to estimate 3D motion patterns via thin-plate-spline interpolation that are used to compensate for respiratory motion. While this method does not require segmentation in 3D, the estimated motion is valid only within a narrow target region around the diaphragm. More recent, Sindel et al. [19] extended this approach by tracking not only the motion of the diaphragm but also a vessel bifurcation to achieve a more reliable motion estimation within the liver. Whilst achieving substantial improvements in reconstruction image quality, the method requires manual tracking of the bifurcation over the complete sequence, making its application cumbersome and time consuming.

2. Materials and Methods

In this work, we propose a novel method to compensate for residual respiratory motion in rotational angiography acquisitions. The main contribution of our method is a 2D 3D registration of the contrasted hepatic vasculature. To this end, the 3D vessel tree, extracted from an uncompensated reconstruction, is forward projected and registered to the 2D projection images. Motion is expressed using a B-spline-based motion model, which is able to account for both rigid translational and non-rigid motion. We evaluate the method on two datasets: a porcine model and a clinically acquired dataset. Evaluation is performed qualitatively and quantitatively, using the reprojection error as well as the vessel sharpness.

An overview over the proposed method is shown in Figure 1. The algorithm uses the stack of acquired projections of the contrast enhanced hepatic vasculature that contains intra-scan motion. Before starting the motion estimation using 2D 3D registration, the projection data has to be preprocessed. To this end, the 2D images are reconstructed in a first step in order to obtain a motion-corrupted reconstruction (Step 1). Afterwards, the 3D vessel tree is segmented from this volume (Step 2) and projected onto the 2D images to define the vessel regions. Within these regions, we apply vessel enhancing filters to the acquired 2D projection images (Step 3). Finally, motion is estimated by registration of the 3D vessel tree to the 2D vessel maps (Step 4), yielding the intra-scan motion estimate. By incorporation of this estimate in the reconstruction, a motion-compensated reconstruction is obtained (Step 5).

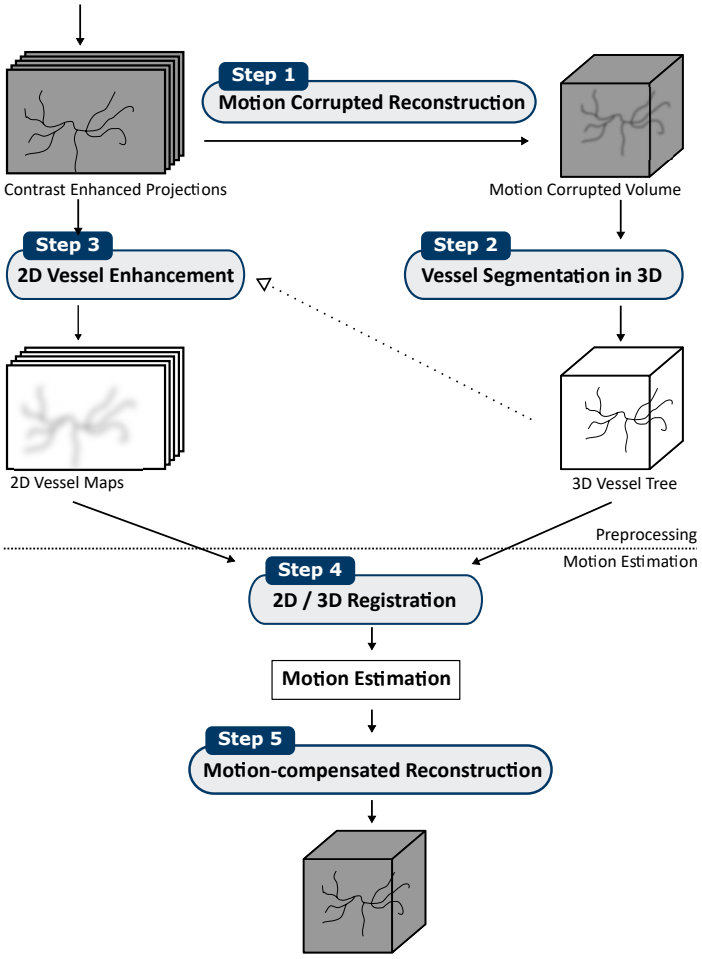

Figure 1: Illustration of the processing pipeline for respiratory motion-compensated 3D reconstruction.

2.1. Data

The data used in this work are from a rotational cone-beam C-arm angiography acquisition. In such a setup, the X-ray source and detector are mounted on a C-shaped gantry that rotates around the patient on a circular trajectory. While acquiring projection images of the liver from di erent angles an iodine-based contrast agent is injected into the hepatic vasculature that selectively contrasts the vessel lumen.

In this work, two sequences were acquired using the same imaging protocol that consist of 396 projection images acquired over 200 on a circular source trajectory over approximately 6 s. Each projection image has 620 480 pixels with an isotropic pixel size of 0 616 mm. During acquisition, contrast agent was injected with a power injector (Medtron, Saarbrücken, Germany) into the hepatic artery. All reconstructions are performed on a voxel grid of 448 448 448 voxels with an isotropic voxel size of 0 5 mm.

The first dataset (D1) is taken from an animal study on a porcine model. This dataset shows substantial respiratory motion that is also observable in projection domain. The second dataset (D2) shows a clinical dataset scanned during breath-hold. In this case, we observe residual respiratory motion only that still decreases image quality and diagnostic value.

2.2. Motion-corrupted Reconstruction

In the first step, an uncompensated and thus motion-corrupted 3D reconstruction is performed that still contains artifacts since intra-scan motion is not compensated for. Reconstruction is achieved using the well-known Feldkamp-Davis-Kress algorithm (FDK), an approximate filtered back-projection type inversion algorithm to the X-ray transform [20]. This algorithm first filters the projection images and then back-projects them to the 3D domain. To this end, each projection image is filtered with a cosine filter [6], multiplied with Parker redundancy weights [21], and finally ramp filtered row-wise. These filtered images are then back-projected along the known cone-beam geometry. We use an implementation similar to Scherl et al. [22] that speeds up the filtering and back-projection steps by parallelizing the algorithm. The reconstructed 3D image then serves as input to vessel segmentation in 3D.

2.3. Vessel Segmentation in 3D

In the motion-corrupted 3D reconstruction, the vessel tree has to be segmented (cf. Figure 1, Step 2). The vessel segmentation in 3D is based on two processing steps: at first, the vessels are enhanced using common vessel enhancement filtering. This results in a pixel wise response in the images that contain the possibility of being a vessel. In a following segmentation step a connected vessel tree is extracted. These two steps are described briefly in the following.

Vessel Enhancement. Contrasted vessels appear as narrow tubular structures that are bright with respect to the background. A common approach to enhancing structures that exhibit this property is based on an Eigenvalue analysis of the Hessian matrix. To obtain consistent enhancement over a wide range of vessel sizes multi-scale filtering has been found beneficial. The idea behind multi-scale image analysis is to transform the original image into a set of derived images by convolution with Gaussian kernels of increasing standard deviation. Consequently, lower and higher scales are useful for the detection of tubular structures with smaller and larger diameters, respectively [23, 24]. The results of di erent scales are then merged to the final filter result using a maximum operation. The result of this operation is a vesselness response. This can be implemented in 2D as well as in 3D. See [25, 26, 27] for implementation details.

Vessel segmentation. The resulting vesselness response map is then used to extract a connected graph that represents the 3D vessel tree. We use region growing based on the fast marching algorithm [28, 29] to extract the centerlines via back-tracking [30]. Within the fast marching step, time values are assigned to all nodes that depend on the choice of speed function and root node. Note, that we used the inverse of the vesselness response as the speed function. This is because we consider vessel centerlines to be cheapest paths, but the vesselness response according to Sato et al. [31] is highest for points likely to correspond to a vessel and low for the background. Then, the root node is selected as the point with minimal speed, i. e. maximal vesselness response, that is considered to lie on the vessel tree or the inflow catheter. The cost of each node is then updated during fast marching. The value of a particular node depends on all neighborhood node values and can be understood as the time necessary to reach this node within the graph. See [29, 30] for more implementation details. The correct endpoints of vessels are not known, however, endpoint candidates for all extractable vessel segments can be estimated during the forward pass. From all possible end points, backtracking is performed towards the root node to extract candidate vessels path. As the resulting centerline tree may still contain erroneous branches, we prune branches that are shorter than a heuristically defined threshold (set to 5.0 mm). Finally, we are left with a linked set of 3D points that represents the hepatic artery tree and inflow catheter.

2.4. Vessel Enhancement 2D

For the 2D 3D registration, the vessels in the 2D projection have to be enhanced as well (cf. Figure 1, Step 3). To this end, the already segmented 3D vessel tree is used to define the vessel regions in 2D by forward projecting the bounding box of the 3D vessel tree. Then, the vessel enhancement filter is only applied within these regions. The same vesselness filter by Sato et al. [31] is utilized to enhance vessels in the 2D projection images. As the final result, we obtain the vessel enhanced images that store, at every pixel, the inverse of the vesselness response.

2.5. 2D 3D Registration

In order to estimate intra-scan respiratory motion, a 2D 3D registration of the 3D vessel tree to the 2D vesselness enhanced projection images is used (cf. Figure 1, Step 4). To this end, the 3D vessel tree is projected under the influence of a motion model onto the 2D enhanced projection image. We accumulate the inverse of the vesselness response and use this as the quality measure in the objective function. This principle is shown schematically in Figure 2. In the following paragraphs, this registration is described in more detail: we start by explaining our motion model based on B-splines, which is able to account for non-rigid or translational motion. Afterwards, we describe the objective function used to assess the quality of a motion model estimate. Finally, we provide further insight in optimization and implementation details.

Motion Models. We investigate two motion models to estimate respiratory motion, namely rigid 3D translational and non-rigid motion. Rather than optimizing for the absolute 3D positions of centerline points at a particular time frame, we optimize for a relative shift from the initial position that is extracted from the uncompensated reconstruction. In this framework, rigid 3D translations are di erent from free-form deformations only in

the constraint that all points exhibit the same, global, displacement.

Non-rigid Motion Model: 3D translational motion is compounded by displacements in cranial-caudal, anterior-posterior, and in left-right direction corresponding to shifts along the $\boldsymbol{e}_x$, $\boldsymbol{e}_y$, and $\boldsymbol{e}_z$ direction, respectively. Displacements in these directions due to respiratory motion are expected to be smooth over time. Consequently, rather than estimating a displacement vector for each of the K projection images independently, shifts for a particular image are sampled from a B-spline. This concept has also been applied recently in di erent applications [32, 33]. Sampling on B-splines has the advantage that the dimensionality of the problem decreases and furthermore the estimated motion is smooth. Moreover, the number of parameters does not depend on the amount of acquired images but on the number of control points used for the spline.

The displacement $\boldsymbol{t}_i^j \in \mathbb{R}^3$ for centerline point j and image i arises from interpolating a 3D spline at the normalized time point $^i\kappa$. It is given by

$$\boldsymbol{t}_i^j(\quad) \quad \sum_{a\ 1}^{A} \ {}_a^j \ B_{a\,d}\ \frac{i}{K} \tag{1}$$

where $B_{a\,d}$ are the B-spline basis functions of degree d. Moreover, $^j\, j \quad 1 \quad N \quad {}_a^j\, j \quad 1 \quad N\ a \quad 1 \quad A$ is the comprehensive set of control points, where $^j \quad {}_a^j \in \mathbb{R}^3\ a \quad 1 \quad A$, again, is a set of A control points, the position of which determines the displacements over the projection sequence for centerline point j. Finally, we introduce $(\quad)$ $\boldsymbol{t}_i^j(\quad)\ i \quad 1 \quad K\ j \quad 1 \quad N$ that contains the displacements for all 3D centerline points $\boldsymbol{p}_j$ to every time point i. The number of displacements that have to be recovered to determine the overall non-rigid motion of the vessel tree is $N \quad A$.

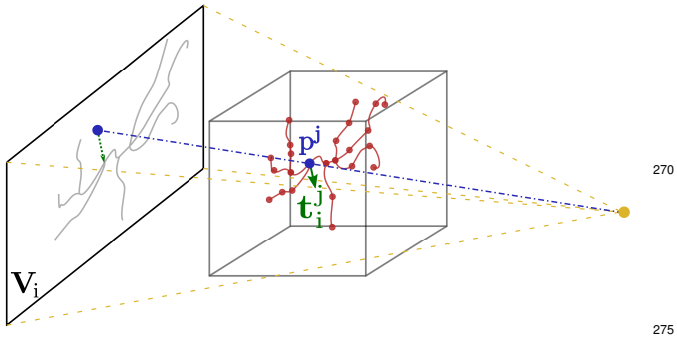

Figure 2: Schematic overview of 2D 3D registration where we show the notation exemplary for a single point: A 3D centerline point $\boldsymbol{p}^j$ (blue) is forward projected into view i. Optimization of Equation 2 yields 3D displacements $\boldsymbol{t}_i^j$ (green) for every centerline point such that the projection of the displaced 3D centerline is in agreement with the observed and vesselness filtered image $\boldsymbol{V}_i$.

Rigid Translational Motion Model: A rigid 3D translational displacement of the complete vasculature follows immediately from the above formulation of non-rigid deformation of the 3D vessel tree. For rigid translational motion, the control point positions ^{j} are the same for every centerline point j such that a single B-spline is su cient to describe this global motion. In that case, the number of control point displacements that need to be estimated reduces substantially from $N \quad A$ to A.

Objective Function. Now we can define the objective function with the following inputs: a stack of 2D vessel maps, the corresponding 3D vessel tree, and one of the motion models described above. Given a particular configuration of control points that describes the overall displacements $(\quad)$, the target energy function $E(\quad)$ assessing the quality of the current estimate is defined as:

$$E(\quad) \quad E_{\text{data}}(\quad) \quad E_{\text{smooth}}(\quad) \tag{2}$$

where $E_{\text{data}}(\quad)$ enforces data fidelity and $E_{\text{smooth}}(\quad)$ encodes neighborhood constraints.

The data fidelity term is derived from the reprojection of the 3D model onto the enhanced projections:

$$\begin{aligned} E_{\text{data}}(\quad) \quad & \sum_{i\ 1}^{K} \sum_{j\ 1}^{N} \boldsymbol{V}_i(\boldsymbol{u}_j^i(\quad)) \\ & \boldsymbol{p}_i^j \quad \boldsymbol{p}^j \quad \boldsymbol{t}_i^j(\quad) \\ & \boldsymbol{u}_j^i(\quad) \quad h(\boldsymbol{P}_i \ \underline{\boldsymbol{p}_j^j}) \end{aligned} \tag{3}$$

where $\boldsymbol{V}_i$ are the vesselness filtered 2D projections and $\boldsymbol{P}_i \in \mathbb{R}^{3\ 4}$ is the projection matrix for frame i that describes the projective mapping from 3D coordinate system to 2D image coordinates. We use underline notation to denote representation in homogeneous coordinates and define function $h(\ )$ that reverses this mapping.

Control points that are close both spatially and temporally are expected to move similarly. The spatial component of this constraint is not meaningful in the purely translational case, but promotes preservation of local topology when non-rigid deformations are considered. It reads:

$$E_{\text{smooth}}(\quad) \quad \sum_{(\ {}_a^j \ {}_b^l)} \ {}_a^j \quad {}_b^l \ {}_2 \tag{4}$$

where $\quad_2$ is the l^2-norm, and $\quad$ is the set of neighboring pairs of control points. Spatial and temporal regularization is achieved by adding control point pairs $(\ {}_a^j \quad {}_a^l)$ over the complete sequence $a \quad 1 \quad A$ if the distance between the corresponding centerline points $\boldsymbol{p}_j$ and $\boldsymbol{p}_l$, respectively, is below 5 0 mm.

For optimization of the motion model, it is crucial to assess changes in total energy E due to displacement of a particular control point ${}_a^j \quad$. To this end, we introduce ${}_a^j$ to denote $\quad$ with all elements held constant except for ${}_a^j$. Then, the energy at the new configuration is computed according to Equation 2 as $E(\quad {}_a^j)$.

Optimization. Gradient- and grid search-based optimization of Equation 2 is, in general, impractical due to the complex shape and high-dimensional domain of the target function, respectively. However, when exchanging continuous control point locations ${}_a^j$ with discrete candidates $(\ {}_a^j)_f$, Equation 2 takes a form that can be optimized e ciently using the $\quad$-expansion algorithm [34]. Rather than directly obtaining optimal control

point positions that minimize the energy, we recover a labeling $\boldsymbol{f} \quad (f_1 \quad f_M)$, where $M \quad K \quad A$ for non-rigid and $M \quad A$ for the translational motion model, respectively, that is optimal with respect to Equation 2.

At one iteration of the algorithm for all candidate labels $1 \quad F$ we seek to find $\hat{\boldsymbol{f}}$ such that

$$\hat{\boldsymbol{f}} \quad \arg\min_{\boldsymbol{f}} E(\quad_{\boldsymbol{f}}) \tag{5}$$

where $\hat{\boldsymbol{f}}$ is within one -expansion of the current labeling $\boldsymbol{f}$. As for particular control points $(\ {}^{j}_{a})_f$ the label f either changes to or stays the same, each move is essentially a partitioning problem that is solved using a graph cut. A comprehensive description of the algorithm can be found in [35, 34]. It is worth mentioning that a single expansion move requires M cost function evaluations (assuming that the current value was stored). However, these evaluations can be parallelized e ciently as changes to a particular control point are evaluated independently from the others.

Implementation Details. The -expansion algorithm traverses the discretized space and accepts updates that reduce the total energy. Consequently, shifts that yield improvement must lie within the capture range of the optimizer, suggesting that the considered label space must be su ciently large. To allow for large motion amplitudes while preserving details, we apply optimization on multiple scales by increasing the number of control points. For rigid motion, displacements are initialized to yield zero shift. Optimization is applied on two scales having 3 and 6 control points each. Shifts are discretized within a cube of $3\,\mathrm{mm}^3 \quad 3\,\mathrm{mm}^3 \quad 3\,\mathrm{mm}^3$. Optimization for non-rigid deformations is initialized with the purely translational estimate. Optimization is performed on a single resolution level with 6 control points expressing deformation over time. As smaller displacements are expected, the discrete samples lie within a cube of $1\,\mathrm{mm}^3 \quad 1\,\mathrm{mm}^3 \quad 1\,\mathrm{mm}^3$ with $5 \quad 5 \quad 5$ samples in each direction. Clamped quadratic B-splines in uniform parameterization were used.

2.6. Motion-compensated Reconstruction

In the last step (cf. Figure 1, Step 5), the motion estimate is used and incorporated into the reconstruction step. Depending on the selected motion model, the compensation step is di erent.

Compensation with the Rigid Translational Motion Model. As the estimated motion is global, it can be conveniently integrated into the projection matrices $\boldsymbol{P}_i \quad \mathbb{R}^{3\ 4}$ that describe the projective mapping from 3D coordinate system to 2D image coordinates of the i-th frame. A motion-compensated version of the projection matrix can then be obtained by

$$\boldsymbol{P}_i^{\mathrm{comp}} \quad \boldsymbol{P}_i \quad \boldsymbol{T}_i \quad \boldsymbol{P}_i \quad \begin{array}{c|c} \boldsymbol{R}_i & \boldsymbol{t}_i \\ \boldsymbol{0} & 1 \end{array} \tag{6}$$

This formulation, in principle, allows for 3D rotations $\boldsymbol{R} \quad \mathbb{R}^{3\ 3}$ and translations $\boldsymbol{t} \quad \mathbb{R}^3$. In the presented case where only translations are considered, $\boldsymbol{R}_i \quad \boldsymbol{R} \quad 1_3$ is the 3D identity mapping. These updated matrices are then used for motion-compensated reconstruction as described for the uncompensated reconstruction in Step 1.

Compensation with the Non-rigid Motion Model. The non-rigid motion estimation by the algorithm devised above is local and, hence, cannot be integrated into the projection geometry directly. Consequently, we use an approach similar to Schäfer et al. [36] that is a voxel-driven, back-projection type algorithm that uses a dense displacement vector field to compensate for motion during reconstruction. Consequently, similar to the uncompensated and rigid motion-compensated reconstruction algorithms, it operates on the pre-filtered projection images.

As mentioned before, displacement vectors are only known at a very limited number of sample positions that correspond to the vascular tree. This information is too sparse to be used for reconstruction and has to be interpolated to accommodate the complete volume of interest. This interpolation is achieved via 3D thin-plate-spline (TPS) warping, that has previously been found beneficial for similar tasks [18, 37, 38]. To constrain the deformation outside the estimated region, we added the corners of the 3D bounding box of the vessel tree to the control points and assigned a zero-displacement.

The displacement fields obtained via TPS interpolation $\boldsymbol{d}_i(\boldsymbol{x})$ are then integrated into the back-projection algorithm by updating the 3D positions prior to projection. As for the optimization of non-rigid motion, we use the translational motion corrected matrices for the reconstruction.

3. Experiments and Results

3.1. Evaluation Methodology

We evaluate the results of the rigid translational and the non-rigid motion estimation algorithms both qualitatively and quantitatively. For qualitative evaluation, representative slices of the uncompensated and both compensated reconstructions are selected by medical imaging experts and visually compared regarding vessel visibility and sharpness.

For quantitative evaluation, we computed the reprojection error of the reconstructed 3D vessel tree. The reprojection error measures the distance of a projected 3D point to the closest observed 2D points in that view [27]. In our case, we measure the distance between the projection of a 3D point of the vessel tree to the closest observation on the 2D detector image that belongs to the 2D vessel centerline. As the true 2D centerline is not known, we manually annotated the 2D vessel centerlines in 10 projection images, which were selected uniformly from the projection stack, to serve as the reference standard. The mean and maximum reprojection errors are then computed by accumulating the mean and maximum error over all views for each 3D centerline point. As a second quantitative measure, we use vessel sharpness available in the CoroEval framework [39]. Put concisely, vessel sharpness measures the contrast of bright tubular structures. We use the CoroEval tool to compute vessel sharpness along the common and right hepatic artery. We expect lower vessel sharpness measures for

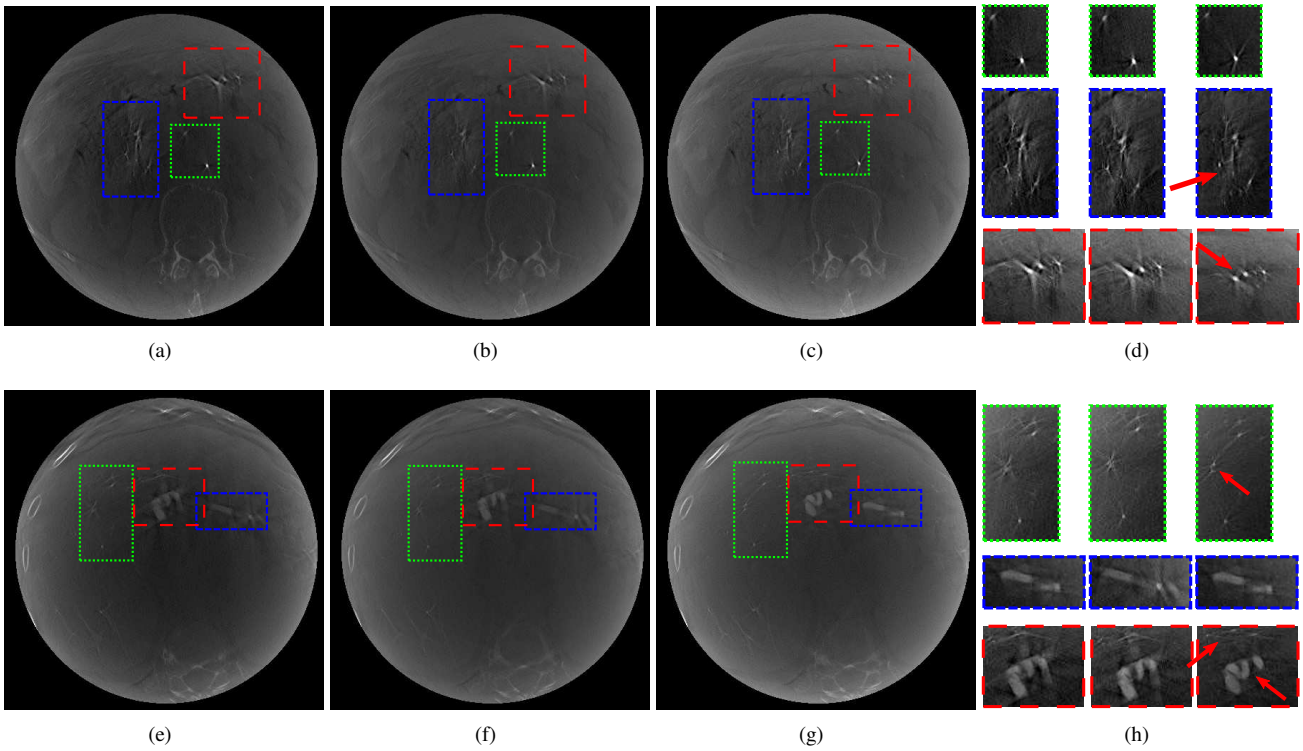

Figure 3: Qualitative results for dataset (D1) showing the porcine model. Figure 3(a-c) and (e-f) show corresponding slices of a 3D volume reconstructed using an uncompensated geometry in (a,e), and the translational and non-rigid motion-compensated geometry in (b,f) and (c,g), respectively. Further, Figure 3(d,h) show magnifications of the regions of interest (ROIs) that are highlighted by colored boxes. The images are shown in a HU window ranging from [-500, 500] while the crops to the ROI are shown in a narrower window [-400, 300].

uncompensated, motion-corrupted reconstructions where intra-scan motion degrades image quality and higher vessel sharpness values for motion-compensated reconstructions. The vessel sharpness ranges between 0 % and 100 % with higher values indicating better performance. It is worth mentioning that, as the magnitude of the measure depends on both vessel sharpness and the contrast level, a comparison of sharpness values between di erent datasets do not necessarily allow for conclusions about reconstruction performance as the contrast level may be di erent.

We then assess these measurements on (a) the uncompensated extracted centerline tree, (b) the vessel tree after translational correction, and (c) after correction for translational and non-rigid motion.

3.2. Results

For qualitative evaluation of the results, representative slices in reconstructed volumes that were obtained using the uncompensated and motion-compensated tomographic reconstruction are shown in Figure 3 and Figure 4 for the first (D1) and second (D2) dataset, respectively. Reconstructed volumes were scaled to obtain intensity values in the conventional Hounsfield Units (HU) range [40]. However, due to severe cupping artifacts resulting from scatter and lateral truncation, the HU values stated in Figure 3 and Figure 4 are only approximate [41]. A wide window was used for the full field of view while the magnified regions of interest (ROIs) are shown with a narrow window to better appreciate the e ects of motion compensation.

Improvements in reconstruction quality are observable for the compensated reconstructions that present as a reduction of streaking artifacts and an increase in vessel sharpness. As expected, the improvements are more pronounced for D1 due to a higher level of intra-scan motion. We use red arrows in the magnified ROIs to highlight areas where aforementioned improvements can be appreciated.

The above observations are also reflected in the mean and maximum reprojection errors for the uncompensated as well as both motion-compensated scenarios that are shown in Table 1 For D1, the averaged 2D mean (maximum) reprojection error for the uncompensated reconstruction reduced by 7 2 % (10 2 %) when translational and by 14 4 % (15 9 %) when non-rigid motion compensation was used, respectively. When considering D2, the same figures of merit improved by 0 7 % (2 0 %) and 3 9 % (6 4 %) when translational and deformable motion compensation was applied.

Results of the quantitative vessel sharpness assessment along the common and right hepatic artery are presented in Table 2. We observe larger improvements for D1 compared to D2 with non-rigid motion compensation outperforming the translational motion compensation and uncompensated reconstruction in both cases. These observations are in very good agreement with both the qualitative assessment as well as the reprojection errors reported above.

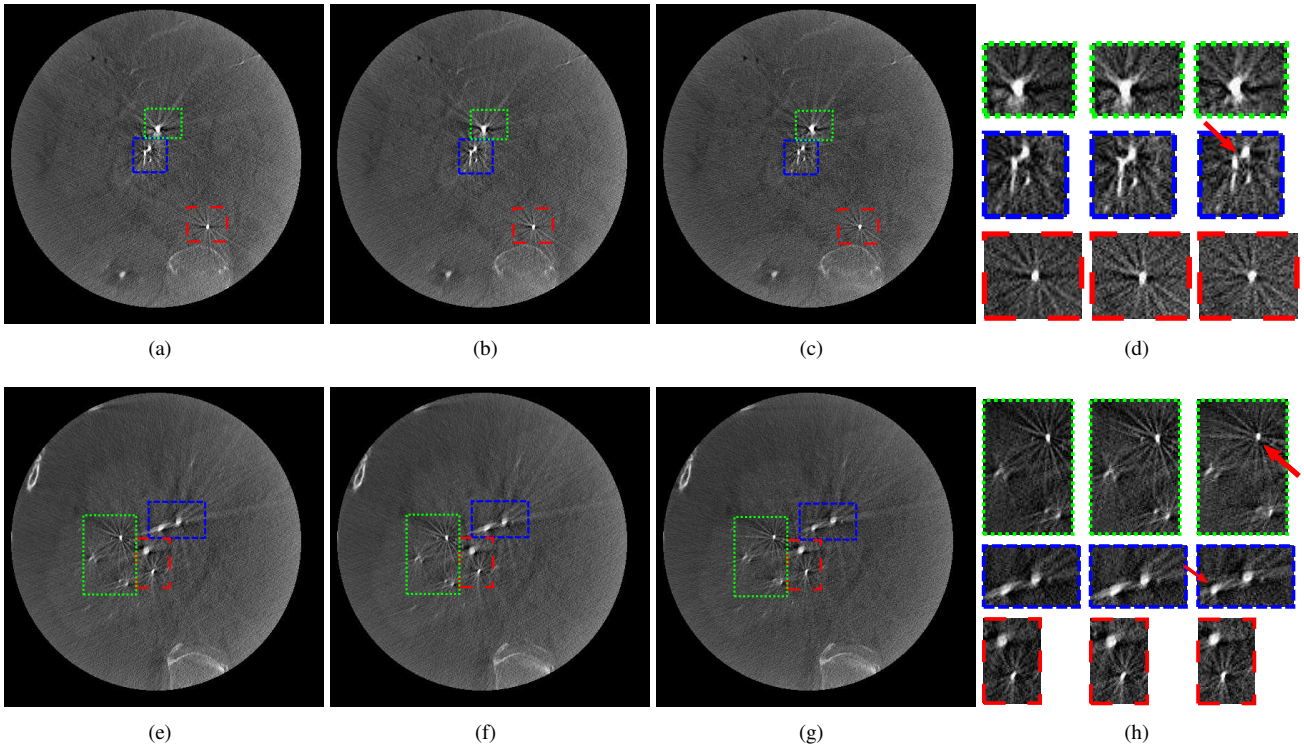

Figure 4: Qualitative results for dataset (D2) that shows reconstructions of a patient: The images show the (a,e) uncompensated, (b,g) the rigidly motion-compensated, and (c,f) the non-rigidly motion-compensated reconstruction. Images in (d,h) are zooms to ROIs highlighted as colored boxes. The images are shown in a HU window ranging from [-600,1000] while the crops are in a narrower window [-300, 900].

Table 1: Averaged mean and maximum reprojection error for the uncompensated geometry, and the updated geometry that was corrected for 3D translational and non-rigid motion, respectively.

	Error [mm]	D1		D2	
Uncompensated	Mean	1 53	0 72	1 54	0 60
	Maximum	3 84	2 42	3 46	2 01
Rigid	Mean	1 42	0 71	1 53	0 59
	Maximum	3 45	2 16	3 39	1 96
Non-rigid	Mean	1 31	0 70	1 48	0 50
	Maximum	3 23	2 04	3 24	1 83

Table 2: Vessel sharpness along the common and right hepatic artery computed using the CoroEval framework [39]. Higher values correspond to increased contrast and improved vessel sharpness.

	D1	D2
Uncompensated	23 %	41 %
Rigid	25 %	41 %
Non-rigid	28 %	42 %

4. Discussion

As mentioned previously, we observed more substantial improvements for the first (D1) than for the second dataset (D2). The dominant reason is that the corruption due to respiratory motion is more severe in D1 compared to D2. This line of argumentation is supported by the observation that purely translational motion compensation only marginally improved the reprojection error for D2, while it had a notable impact on the reprojection error for D1.

The overall magnitude of vessel sharpness is lower for D1 compared to D2 suggesting lower vessel contrast that is also reflected in the HU windows used for display in Figure 3 and Figure 4, respectively.

We noticed a delayed contrast bolus injection in dataset D2 such that the arterial tree is not fully visible in the first projections of the sequence. This introduces additional streaking artifact [42] that cannot be compensated for by the proposed methods that address inconsistencies due to intra-scan motion only.

From Figure 3 and Figure 4 it becomes apparent that, despite the quantitative improvements of the translational compensation, notable reduction of streaking artifacts as well as improved vessel sharpness and separation is only achieved when non-rigid motion is considered. Our formulation of motion, in which every 3D centerline point is considered as a B-spline over time, naturally accounts for translational and rigid motion. Yet, intermediate motion models, such as a ne transformations, paired with stochastic gradient descent optimization [43] could be investigated in future work.

The proposed methods rely on registration of a 3D vasculature model, which is extracted from an uncompensated reconstruction, to the vesselness enhanced 2D projection images. Consequently, the estimated motion reliably reflects artery motion only at centerline points suggesting that the extracted 3D vessel tree ideally contains all contrasted vessels. In presence of substantial corruption by high-amplitude respiratory motion and

thus artifact, an uncompensated reconstruction may not allow for the extraction of 3D artery centerlines of su cient quality particularly in regions close to the diaphragm where respiratory motion is strongest. In such scenarios, an iterative scheme of the proposed method is conceivable where the 3D vessel tree is refined with increasingly reliable motion estimates.

The quantitative measures reported here are relative as they do not only account for inconsistencies due to intra-scan motion but are also a ected by (a) incorrectly extracted 3D centerline branches and (b) the quality of the manually annotated 2D ground-truth. Erroneously extracted branches in 3D result in a systematic o set of the reprojection error, while small deviations in centerline annotation yield statistic fluctuations. More importantly, the maximal response of the vessel enhancing filters, and thus the target of the proposed 2D 3D registration, is not guaranteed to coincide with the true vessel centerline that is estimated during manual annotation. Consequently, these sources of error impose a fundamental lower bound on the reprojection error used for assessment.

The current evaluation is limited to two datasets and it needs to be evaluated how well our findings generalize to a larger population. However, the proposed formulation of fully automatic deformable motion estimation and compensation may be of broader interest, e. g., in coronary angiography where rigid 2D 3D registration of prior models to the acquired image sequence is part of the state-of-the-art [44, 45].

5. Conclusions

We proposed automated methods for translational and non-rigid respiratory motion compensation in cone-beam rotational hepatic angiography. The methods are based on registration of the 3D vascular tree that is extracted from an uncompensated reconstruction to vessel enhanced versions of the projection images. We found improvements in image quality that, qualitatively, lead to fewer streaking artifacts and better vessel contrast, and, quantitatively, to a reduction of both mean and maximum reprojection error as well as increased vessel sharpness.

Intra-scan respiratory motion estimation remains a challenging problem in cone-beam rotational angiography as it is low frequency but potentially of high amplitude. Consequently, future work will focus on deriving motion correction algorithms that do not require initial 3D models but exploit image-based data corruption metrics, such as consistency conditions or autofocus measures.

Acknowledgements

The authors gratefully acknowledge funding support from the NIH Shared Instrument Grant S10 RR026714 supporting the zeego@StanfordLab. Special thanks also go to Assoc. Prof. Nishita Kothary, MD from the Department of Radiology, Stanford University Medical Center for providing the clinical data.

Conflicts of Interest

The authors have no conflicts of interest to disclose.

References

[1] J. M. Llovet, M. I. Real, X. Montaña, R. Planas, S. Coll, J. Aponte, C. Ayuso, M. Sala, J. Muchart, R. Solà, et al., Arterial embolisation or chemoembolisation versus symptomatic treatment in patients with unresectable hepatocellular carcinoma: a randomised controlled trial, The Lancet 359 (9319) (2002) 1734–1739.

[2] D. B. Brown, J.-F. H. Geschwind, M. C. Soulen, S. F. Millward, D. Sacks, Society of interventional radiology position statement on chemoembolization of hepatic malignancies, Journal of vascular and interventional radiology 17 (2) (2006) 217–223.

[3] S. Virmani, R. K. Ryu, K. T. Sato, R. J. Lewandowski, L. Kulik, M. F. Mulcahy, A. C. Larson, R. Salem, R. A. Omary, E ect of C-arm angiographic CT on transcatheter arterial chemoembolization of liver tumors, Journal of Vascular and Interventional Radiology 18 (10) (2007) 1305–1309.

[4] Y.-X. J. Wang, T. De Baere, J.-M. Idée, S. Ballet, Transcatheter embolization therapy in liver cancer: an update of clinical evidences, Chinese Journal of Cancer Research 27 (2).

[5] J. Iwazawa, S. Ohue, T. Mitani, H. Abe, N. Hashimoto, M. Hamuro, K. Nakamura, Identifying feeding arteries during TACE of hepatic tumors: comparison of C-arm CT and digital subtraction angiography, American Journal of Roentgenology 192 (4) (2009) 1057–1063.

[6] G. L. Zeng, Medical Image Reconstruction, Springer, 2010.

[7] S. Miyayama, M. Yamashiro, M. Okuda, Y. Yoshie, N. Sugimori, S. Igarashi, Y. Nakashima, O. Matsui, Usefulness of cone-beam computed tomography during ultraselective transcatheter arterial chemoembolization for small hepatocellular carcinomas that cannot be demonstrated on angiography, Cardio Vascular and Interventional Radiology (32) (2009) 255–264.

[8] L. Pung, M. Ahmad, K. Mueller, J. Rosenberg, C. Stave, G. Hwang, R. Shah, N. Kothary, The role of cone-beam ct in transcatheter arterial chemoembolization for hepatocellular carcinoma: A systematic review and meta-analysis, Journal of Vascular and Interventional Radiology (28) (2017) 334–341.

[9] M. Von Siebenthal, Analysis and Modelling of Respiratory Liver Motion Using 4DMRI, Ph.D. thesis, Citeseer (2008).

[10] M. Unberath, A. Aichert, S. Achenbach, A. Maier, Consistency-based respiratory motion estimation in rotational angiography, Medical Physics 44 (9) (2017) e113–e124.

[11] A. Tognolini, J. D. Louie, G. L. Hwang, L. V. Hofmann, D. Y. Sze, N. Kothary, Utility of C-arm CT in Patients with Hepatocellular Carcinoma undergoing Transhepatic Arterial Chemoembolization, Journal of Vascular and Interventional Radiology 21 (3) (2010) 339–347.

[12] A. Tognolini, J. Louie, G. Hwang, L. Hofmann, D. Sze, N. Kothary, C-arm Computed Tomography for Hepatic Interventions: A Practical Guide, Journal of Vascular and Interventional Radiology 21 (12) (2010) 1817–1823.

[13] T. Geimer, M. Unberath, O. Taubmann, C. Bert, A. Maier, Combination of Markerless Surrogates for Motion Estimation in Radiation Therapy, in: Proc. Computer Assisted Radiology and Surgery (CARS), 2016.

[14] M. Wilms, R. Werner, J. Ehrhardt, A. Schmidt-Richberg, H. Schlemmer, H. Handels, Multivariate regression approaches for surrogate-based diffeomorphic estimation of respiratory motion in radiation therapy, Physics in Medicine and Biology 59 (5) (2014) 1147.

[15] J. M. Balter, L. A. Dawson, S. Kazanjian, C. McGinn, K. K. Brock, T. Lawrence, R. Ten Haken, Determination of Ventilatory Liver Movement via Radiographic Evaluation of Diaphragm Position, International Journal of Radiation Oncology* Biology* Physics 51 (1) (2001) 267–270.

[16] J. Sonke, L. Zijp, P. Remeijer, M. van Herk, Respiratory correlated cone beam CT, Medical physics 32 (4) (2005) 1176–1186.

[17] D. Schäfer, M. Lin, P. Rao, R. Lo roy, E. Liapi, N. Noordhoek, P. Eshuis, A. Radaelli, M. Grass, J.-F. Geschwind, Breathing Motion Compensated Reconstruction for C-Arm Cone Beam CT Imaging: Initial Experience Based on Animal Data, in: SPIE Medical Imaging, International Society for Optics and Photonics, 2012, pp. 83131D–83131D.

[18] M. Bögel, H. G. Hofmann, J. Hornegger, R. Fahrig, S. Britzen, A. Maier, Respiratory Motion Compensation Using Diaphragm Tracking for Cone-Beam C-Arm CT: A Simulation and a Phantom Study, International Journal of Biomedical Imaging 2013 (2013) 10.

[19] A. Sindel, M. Bögel, A. Maier, R. Fahrig, J. Hornegger, A. Dörfler, Res-

piratory Motion Compensation for C-Arm CT Liver Imaging, in: Bildverarbeitung für die Medizin, Springer, 2015, pp. 221–226.

[20] L. A. Feldkamp, L. C. Davis, J. W. Kress, Practical Cone-Beam Algorithm, J. Opt. Soc. Am. A 1 (6) (1984) 612–619.

[21] D. L. Parker, Optimal Short Scan Convolution Reconstruction for Fan Beam CT, Medical physics 9 (2) (1982) 254–257.

[22] H. Scherl, B. Keck, M. Kowarschik, J. Hornegger, Fast GPU-Based CT Reconstruction using the Common Unified Device Architecture (CUDA), in: Nuclear Science Symposium, Medical Imaging Conference 2007, Vol. 6, IEEE, Honolulu, HI, United States, 2007, pp. 4464–4466.

[23] K. Drechsler, C. Laura, Comparison of Vesselness Functions for Multiscale Analysis of the Liver Vasculature, in: 10th IEEE International Conference on Information Technology and Applications in Biomedicine, 2010, pp. 1–5.

[24] A. Kerkeni, A. Benabdallah, M. H. Bedoui, Coronary Artery Multiscale Enhancement Methods: A Comparative Study, in: International Conference Image Analysis and Recognition, Springer, 2013, pp. 510–520.

[25] T. M. Koller, G. Gerig, G. Szekely, D. Dettwiler, Multiscale detection of curvilinear structures in 2-D and 3-D image data, in: Computer Vision, 1995. Proceedings., Fifth International Conference on IEEE, 1995, pp. 864–869.

[26] A. Frangi, W. Niessen, K. Vincken, M. Viergever, Multiscale Vessel Enhancement Filtering, in: First International Conference on Medical Image Computing and Computer-Assisted Intervention, 1998, pp. 130–137.

[27] M. Unberath, O. Taubmann, M. Hell, S. Achenbach, A. Maier, Symmetry, outliers, and geodesics in coronary artery centerline reconstruction from rotational angiography, Medical Physics 44 (11) (2017) 5672–5685.

[28] R. Malladi, J. A. Sethian, B. Vemuri, Shape Modeling with Front Propagation: A Level Set Approach, IEEE transactions on pattern analysis and machine intelligence 17 (2) (1995) 158–175.

[29] J. Sethian, Fast marching methods, SIAM review 41 (2) (1999) 199–235.

[30] U. Jandt, D. Schäfer, M. Grass, V. Rasche, Automatic generation of 3D coronary artery centerlines using rotational X-ray angiography, Medical Image Analysis 13 (6) (2009) 846–858.

[31] Y. Sato, S. Nakajima, N. Shiraga, H. Atsumi, S. Yoshida, T. Koller, G. Gerig, R. Kikinis, Three-dimensional multi-scale line filter for segmentation and visualization of curvilinear structures in medical images, Medical Image Analysis 2 (2) (1998) 143–168.

[32] A. Sisniega, J. W. Stayman, J. Yorkston, J. H. Siewerdsen, W. Zbijewski, Motion compensation in extremity cone-beam CT using a penalized image sharpness criterion, Physics in Medicine and Biology 62 (9) (2017) 3712.

[33] M. Unberath, O. Taubmann, B. Bier, T. Geimer, M. Hell, S. Achenbach, A. Maier, Respiratory Motion Compensation in Rotational Angiography: Graphical Model-based Optimization of Auto-focus Measures, in: Proc. International Symposium on Biomedical Imaging (ISBI) 2017, 2017.

[34] Y. Boykov, O. Veksler, R. Zabih, Fast Approximate Energy Minimization via Graph Cuts, IEEE Transactions on pattern analysis and machine intelligence 23 (11) (2001) 1222–1239.

[35] O. Veksler, E cient graph-based energy minimization methods in computer vision, Dissertation, Cornell University (1999).

[36] D. Schäfer, J. Borgert, V. Rasche, M. Grass, Motion-Compensated and Gated Cone Beam Filtered Back-Projection for 3-D Rotational X-Ray Angiography, IEEE Transactions on Medical Imaging 25 (7) (2006) 898–906.

[37] M. Berger, K. Müller, A. Aichert, M. Unberath, J. Thies, J.-H. Choi, R. Fahrig, A. Maier, Marker-free motion correction in weight-bearing cone-beam CT of the knee joint, Medical Physics 43 (3) (2016) 1235–1248.

[38] K. Müller, C. Schwemmer, J. Hornegger, Y. Zheng, Y. Wang, G. Lauritsch, C. Rohkohl, A. Maier, C. Schultz, R. Fahrig, Evaluation of interpolation methods for surface-based motion compensated tomographic reconstruction for cardiac angiographic C-arm data, Medical Physics 40.

[39] C. Schwemmer, C. Forman, J. Wetzl, A. Maier, J. Hornegger, Coroeval: a multi-platform, multi-modality tool for the evaluation of 3d coronary vessel reconstructions, Physics in Medicine & Biology 59 (17) (2014) 5163.

[40] T. Reeves, P. Mah, W. McDavid, Deriving hounsfield units using grey levels in cone beam ct: a clinical application, Dentomaxillofacial Radiology 41 (6) (2012) 500–508.

[41] B. Bier, M. Berger, A. Maier, M. Kachelrieß, L. Ritschl, K. MÃ¼ller, J.-H. Choi, R. Fahrig, Scatter correction using a primary modulator on a clinical angiography c-arm ct system, Medical Physics 44 (9) (2017) e125–e137.

[42] A. Fieselmann, F. Dennerlein, Y. Deuerling-Zheng, J. Boese, R. Fahrig, J. Hornegger, A model for filtered backprojection reconstruction artifacts due to time-varying attenuation values in perfusion C-arm CT, Physics in Medicine and Biology 56 (12) (2011) 3701.

[43] C. Rohkohl, G. Lauritsch, L. Biller, M. Prümmer, J. Boese, J. Hornegger, Interventional 4D motion estimation and reconstruction of cardiac vasculature without motion periodicity assumption, Medical Image Analysis 14 (5) (2010) 687–694.

[44] C. Blondel, G. Malandain, R. Vaillant, N. Ayache, Reconstruction of coronary arteries from one rotational x-ray projection sequence, IEEE Transactions on Medical Imaging 25 (5) (2006) 653–663.

[45] S. Çimen, A. Gooya, M. Grass, A. F. Frangi, Reconstruction of coronary arteries from X-ray angiography: A review, Medical Image Analysis 32 (2016) 46–68.